Title: Electronic nematicity in Sr_2RuO_4

J. Wu[1,*], H. P. Nair[2,*], A. T. Bollinger[1], X. He[1,3], I. Robinson[1], N. J. Schreiber[2], K. M. Shen[4,5], D. G. Schlom[2,5], and I. Božović[1,3]

Affiliations:

[1]*Brookhaven National Laboratory, Upton, New York 11973-5000, USA*

[2]*Department of Materials Science and Engineering, Cornell University, Ithaca, New York 14853, USA*

[3]*Yale University, Applied Physics Department, New Haven CT 06520, USA*

[4]*Physics Department, Cornell University, Ithaca, New York 14853, USA*

[5]*Kavli Institute at Cornell for Nanoscale Science, Ithaca, New York 14853, USA*

*Correspondence to: bozovic@bnl.gov.

†These authors contributed equally.

Abstract:

We have discovered breaking of the rotational symmetry in the electron fluid in unconventional superconductor, Sr_2RuO_4 (SRO). We have measured the angle-resolved transverse resistivity (ARTR), a sensitive indicator of the electronic nematicity, in high-quality superconducting SRO thin films on various substrates. The ARTR signal, heralding the nematicity, is present and substantial already at the room temperature, and grows by an order of magnitude upon cooling down to 4 K. The highest-conductivity direction does not coincide with any crystal axis in SRO films deposited on tetragonal substrates, while on orthorhombic substrates it tends to align with the shorter axis; however, the magnitude of anisotropy stays the same. These are strong indications that the normal state of SRO is electronic nematic.

One Sentence Summary: The normal state of the unconventional superconductor, strontium ruthenate, is electronic nematic.

Main Text:

It has been predicted theoretically that in some unconventional metals the symmetry of the electron fluid can be spontaneously broken, i.e., reduced compared to that of the underlying crystal lattice — the situation referred to as 'electronic nematicity' *(1-7)*. Indeed, transport anisotropy unexpected from the crystal structure has been observed in copper-oxide *(8-17)*, Fe-based *(18-21)*, and heavy-fermions superconductors *(22, 23)*. This brings into focus the interplay between unconventional superconductivity, nematicity, and electron correlations.

Our recent study of a prototypical *d*-wave superconductor, $La_{2-x}Sr_xCuO_4$ (LSCO), using the ARTR method *(17)* revealed that the electric transport in the normal state shows only the twofold rotational symmetry (**C_2**) while the tetragonal crystal lattice has higher, fourfold (**C_4**) symmetry. This deviation from the canonical Fermi liquid behavior in cuprates has been ascribed to strong electron correlations. It is of fundamental interest to explore how widespread the nematic state is and whether it is linked with unconventional superconductivity. We have chosen to start with SRO, since it also is an unconventional superconductor, harbors strong electron correlations, and has the same layered-perovskite (K_2NiF_4) structure as LSCO. Thus, one wonders whether the normal state of SRO, from which the superconductivity emerges, also breaks the rotational symmetry of the lattice, or not.

With this motivation, we have synthesized high-quality single crystal films of (001)-oriented SRO by molecular beam epitaxy *(24-26)*. The best films are superconducting with the critical temperature $T_c \approx 1.5$ K *(26)*. The films were deposited on (001)-oriented $(LaAlO_3)_{0.29}(SrTa_{1/2}Al_{1/2}O_3)_{0.71}$ (LSAT) and (110)-oriented $NdGaO_3$ (NGO) substrates. The film thickness is chosen to be smaller than the critical thickness for relaxation, so the in-plane lattice constants of the films remain the same as those of the underlying substrate. Since LSAT is tetragonal *(27)*, while NGO is orthorhombic *(28)* comparing SRO/LSAT to SRO/NGO enables us to discern the contributions of the lattice distortion to the observed effects. The details on the film synthesis process and the characterization of crystal structures and surface morphology are provided in the Supplement.

To study the nematicity, we have developed a direct and sensitive method, ARTR *(17)*. The lithography pattern we have used is depicted in Fig. 1a. The total of 36 Hall bars are arranged

radially in a 'sunbeam' pattern, with $\Delta\phi = 10^0$ angles between successive Hall bars. The electric current runs along a Hall bar, while longitudinal or transverse voltages are measured using three pairs of evenly-spaced gold contacts, Fig. 1b. The angle $\phi = 0^0$ corresponds to the [100] direction of the SRO lattice. As explained in Ref. 17, if the crystal and the electron fluid both have tetragonal (**C**$_4$) symmetry in-plane, the longitudinal resistivity ρ must be isotropic, and the transverse resistivity ρ_T must be zero by symmetry at every angle. In contrast, if the symmetry of the electron transport is reduced to **C**$_2$, ρ_T must be non-zero except when the current flow is along one of the principal crystal axes. More precisely, both ρ and ρ_T must oscillate as a function of ϕ with the period of 180^0, as follows:

$$\rho(\phi) = \bar{\rho} + \Delta\rho\cos[2(\phi-\alpha)] \qquad (1)$$

$$\rho_T(\phi) = \rho_T{}^0\sin[2(\phi-\alpha)] \qquad (2)$$

where $\bar{\rho} = (\rho_{max} + \rho_{min})/2$, the largest resistivity ρ_{max} is measured along the 'hard' axis oriented at some angle α, the smallest resistivity ρ_{min} is measured along the 'easy' axis at $\phi = \alpha \pm 90^0$, and $\rho_T{}^0 = \Delta\rho = (\rho_{max} - \rho_{min})/2$.

Hence, by measuring $\rho_T(\phi)$ one can detect electronic nematicity. Note that while $\rho(\phi)$ oscillates around some average value $\bar{\rho}$ that can be large, $\rho_T(\phi)$ oscillates around zero and is thus free of such a background signal. This makes the ARTR measurements much more sensitive to the electronic nematicity; its signal-to-noise (limited by the inevitable device-to-device variations due to lithography) is typically better than that of the measurements of $\rho(\phi)$ by about two orders of magnitude. This ARTR method has substantial advantages compared to just measuring the longitudinal resistivity ρ_a and ρ_b along the two principal in-plane crystal directions, e.g., [100] and [010]. This is best illustrated by an example where the easy axis is diagonal, $\alpha = 45^0$. Then one would measure $\rho_a = \rho_b = \bar{\rho}$ and conclude that the sample is isotropic, even if ρ_{max} and ρ_{min} in fact differ by orders of magnitude. In any case, the angular resolution is crucial for determining the director of nematic order, which in general is not aligned with the crystal axes. Even more important, the current flow in the sunbeam pattern is guided in the direction defined by the in-plane orientation of the Hall bar. This is not the case in e.g., van der Pauw method, where the

current flow pattern gets distorted towards the 'easy' axis; this complicates the analysis and can easily produce spurious sign reversals of the ρ_a/ρ_b ratio, as we illustrate in the Supplement.

Using the ARTR technique, we have indeed discovered large-amplitude electronic nematicity in SRO. In Figs. 1c and 1e, we show the ARTR data taken from an SRO/LSAT sample at temperatures T = 295 K and T = 4 K, respectively. In both cases, and at every temperature in between, $\rho_T(\phi)$ oscillates with the period of 180^0 in ϕ, with the sign alternating between positive and negative. All the experimental data of $\rho_T(\phi)$ (solid circles) can be well fitted (the solid red curves in Figs. 1c and 1e) by the simple expression (2) with only two free parameters, the amplitude ρ_T^0 and the phase offset α. In Figs. 1d and 1f, we show the corresponding $\rho(\phi)$ data (blue solid dots). The red dashed curves are not independent fits to these $\rho(\phi)$ data; rather, they are calculated using as an input the values of ρ_T^0 and α inferred from the $\rho_T(\phi)$ data, shifted up by the angle-averaged longitudinal resistivity $\bar{\rho}$ and then left by 45^0. Apparently, the angular oscillations in $\rho(\phi)$ and $\rho_T(\phi)$ have the same amplitude and are phase-shifted exactly as predicted by the formulae (1) and (2). This is an unambiguous manifestation of the uniaxial anisotropy of the electric transport in the *a*-*b* plane.

To make this more intuitive, in Figs. 1g and 1h we plot the same data as in Figs. 1e and 1f, respectively, but in polar coordinates, where the radial distance scales with the $\rho_T(\phi)$ and $\rho(\phi)$ data measured at T = 4 K. The patterns show that the symmetry in the electronic transport is $\mathbf{C}_2$, reduced compared to the $\mathbf{C}_4$ symmetry of the lattice. The 'clover-leaf' shape in $\rho_T(\phi)$ should not be confused with the *d*-wave gap symmetry in the momentum space; this is just a consequence of the existence of easy and hard transport axes in real space, due to the nematic order. This is corroborated by the 'peanut' shape in $\rho(\phi)$, as seen in Fig. 1h.

Comparing the data at T = 4 K and T = 295 K, it is apparent that ρ_T^0 varies with T substantially. In contrast, α remains roughly the same: $\alpha = 68^0$ at T = 4 K and $\alpha = 65^0$ at T = 295 K. Hence, the nematic director is fixed in real space regardless of the sample temperature. It is visually clear in Figs.1g and 1h that the angles at which the values of $\rho_T(\phi)$ or $\rho(\phi)$ peak do not coincide with the principal crystal directions. The fact that the nematic director does not align with the crystal axes rules out the possibility that the observed 'nematicity' simply originates in the anisotropy of the lattice.

It should be emphasized that the angular oscillations in $\rho_T(\phi)$ and $\rho(\phi)$ are not caused by extrinsic factors, e.g. contact misalignment, film inhomogeneity, film thickness variations, etc. We have accessed and ruled out these possibilities by detailed and targeted experiments already (*17*). Nevertheless, to further address the concerns about the lithography process and the measurement setup, here we have fabricated a 'sunbeam" device out of conventional metal (Ti), using the same lithography mask and process. The ARTR measurements on this control sample indeed showed the absence of any angular oscillations in $\rho_T(\phi)$ and $\rho(\phi)$ (see the Supplement for details). This clearly shows that the observed angular oscillations must originate from SRO. On the other hand, the symmetry of the observed patterns (Fig. 1h and Fig. 2f) and the large magnitude of the observed effect eliminate the possibility that they might originate from conceivable small gradients in the film composition or thickness. Having ruled all the experimental artifacts we could think of and check, we conclude that SRO is intrinsically nematic.

To further explore the effects of lattice distortions, for comparison we have also studied SRO films epitaxially grown on (110) NGO, a deliberately chosen orthorhombic substrate. The films were thin enough (23 nm) that the SRO lattice in this case is forced to be orthorhombic by the epitaxial strain. The X-ray diffraction experiments, on the same samples on which $\rho_T(\phi)$ and $\rho(\phi)$ were measured, confirmed this expectation (see the Supplement for details). The *a* and *b* lattice constants differ by 0.5% in the NGO substrate as well as in the SRO films on NGO. In contrast, in the SRO film on LSAT the difference is just 0.03%, more than one order of magnitude smaller. ARTR measurements on SRO/NGO films also revealed strong angular oscillations with the period of 180^0 in both $\rho_T(\phi)$ and $\rho(\phi)$ at $T = 4$ K as well as at $T = 295$ K (Figs. 2a, 2b, 2c and 2d). Like in the SRO/LSAT sample, these $\rho_T(\phi)$ and $\rho(\phi)$ oscillations can be simultaneously well fitted by Eqs. (1) and (2) at a given temperature. The fits yield $\alpha = 7^0$ at $T = 4$ K and $\alpha = 6^0$ at $T = 295$ K. The plots in polar coordinates (Figs. 2d and 2f) show this more intuitively: the in-plane directions corresponding to ρ_{max} and ρ_{min} are nearly parallel to the SRO/NGO crystallographic [100] and [001] directions of SRO, respectively. Note, however, that we have repeated the growth of SRO on (110) NGO substrates multiple times and found that in some samples the nematic director is *not* aligned with either of the crystallographic directions (see the Supplement for details). This indicates that the orthorhombic distortion induced in the SRO lattice by the epitaxial strain from

NGO is barely at the border of being strong enough to pin the orientation of nematicity in the electron fluid.

Turning the focus on the amplitude of nematic order, we explore how it depends on temperature and on the epitaxially-imposed lattice distortion. To facilitate a quantitative comparison, we define the magnitude of the nematicity as $N = \rho_T^0/\bar{\rho}$. In analogy to the Hall angle, N has a geometric interpretation; it is equal to the arctangent of the angle between the directions of the electric field and the current density vectors. Thus, N is an intrinsic quantity characteristic of every nematic material. We measured N continuously as a function of temperature. In both SRO/LSAT and SRO/NGO, $N(T)$ increases rapidly as T decreases (Fig. 3), implying that the nematic order is strengthened as the thermal fluctuations diminish. Thus, the nematic state is not an excited state but a real ground state at zero temperature. Next, one can see that N is nearly equal in SRO/LSAT and SRO/NGO at every temperature, despite more than an order of magnitude difference between the lattice distortions. If the origin of nematicity were in the anisotropy of the lattice, or of the electron-lattice coupling, N should have increased fast with the lattice distortion, in variance with the experimental observations. This is yet another indication that the nematic order in SRO is primarily of electronic origin.

The corresponding temperature-dependent $\rho_T(T)$ and $\rho(T)$, measured at three representative directions, are shown in the Supplement. As the temperature is increased, both $\rho_T(T)$ and $\rho(T)$ increase monotonically. In contrast, $N(T)$ decreases, and one could indeed surmise that it should vanish at some temperature T^*. However, this T^* cannot be measured directly since SRO films lose oxygen and decompose at elevated temperatures. Nevertheless, it is clear that $N(T)$ deviates significantly from the mean-field-like $(T^*\text{-}T)^{1/2}$ dependence; the shape of $N(T)$ is concave instead of convex. Note that the same behavior is seen in LSCO *(17)* in $N(T)$ as well as in other key physical parameters such as the upper critical magnetic field H_{c2}, etc., which has been ascribed to the presence of strong fluctuations over a broad T range.

The next important question is how is nematicity related to superconductivity, and more specifically, whether the nematic amplitude traverses through the superconducting transition smoothly or with some jump or kink at T_c. We have addressed this question in three ways. One is that in SRO superconductivity is sensitive to uniaxial strain *(25)*. The SRO/LSAT film studied in

Fig. 1 is metallic but not superconducting, at least down to T = 300 mK, the lowest temperatures available in our Helium-3 cryogenic setup. In contrast, the SRO/NGO film studied in Fig. 2 has T_c ≈ 0.9 K, as shown in the Supplement. Nevertheless, the amplitudes of nematicity are substantial and nearly equal in SRO/LSAT and SRO/NGO (Fig. 3). The other testing opportunity stems from the fact that unlike the superconductivity in conventional metals, the superconductivity in SRO is very sensitive to even a minor amount of chemical impurities and other structural imperfections. It was reported that as the residual resistivity of SRO increases, T_c decreases sharply to zero *(24)*. Precisely for this reason, it has been an extremely challenging task to synthesize superconducting SRO films. Indeed, SRO films with the growth conditions even slightly off the optimal growth recipe turn out not to be superconducting. We have thus been able to study, for comparison, an SRO/NGO film that has an essentially identical lattice structure and a similar longitudinal resistivity at room temperature as the superconducting film in Fig. 2, but has a somewhat larger residual resistivity and is not superconducting down to T = 0.3 K. ARTR measurement on this sample showed $\rho_T(\phi)$ and $\rho(\phi)$ nearly identical to those shown in Fig. 2 (see the Supplement for details) regardless of the differences in disorder and superconductivity. The third way is to suppress the superconductivity by an external magnetic field and show that this underlying metallic state is also nematic, with both $N(T)$ and $\alpha(T)$ seamlessly connecting to their zero-field dependences above T_c. Altogether, the above shows that the nematic state of SRO is intrinsic and more robust than superconductivity.

The central finding of the present paper is that in SRO, as the temperature is reduced, superconductivity emerges out of the nematic normal state. As for the superconducting state, we have no direct information, since ARTR technique is 'blinded' once the resistance drops to zero, but one can state what seems plausible. The spontaneous breaking of the rotational symmetry in the normal state, as reported here in SRO, probably indicates that the electron-electron interaction is anisotropic in the *a*-*b* plane. If that is the case, the rotationally-symmetric *s*-wave superconducting state may be energetically less favorable. Rather, one would expect the strength of Cooper paring to oscillate with the azimuth angle ϕ, giving rise to a superconducting state with nodes and anti-nodes along different orientations, like in cuprates.

The experimental status of the symmetry of the superconducting order parameter in SRO seems unclear. For many years, SRO has been considered as a candidate for *p*-wave or more generally

for spin-triplet superconductivity (*29-33*). However, a recent NMR experiment indicated that the superconducting order parameter of the superconducting state of SRO is not odd-parity (*34*), hence, not *p*-wave. The new results presented here indicate that the *s*-wave state is also unlikely. Taken together, this narrows the options down, and we hope this may reinvigorate future research and attempts to directly and unambiguously resolve this important question.

In summary, we believe that the ARTR data reported here in SRO, and previously in copper-oxide superconductors, indicate that the unconventional superconductivity and the nematicity may be both ascribed to strong and anisotropic electron correlations. We conjecture that the electronic nematicity may be widespread in strongly correlated materials, and our ARTR technique provides a direct and simple way for its detection and characterization.

References and Notes:

1. J. Zaanen, O. Gunnarsson, Charged magnetic domain lines and the magnetism of high-T_c oxides. *Phys. Rev. B* **40**, 73917394 (1989).
2. J. Zaanen, A. M. Oles, Striped phase in the cuprates as a semiclassical phenomenon. *Ann. Phys.* **5**, 224-246 (1996).
3. S. A. Kivelson, E. Fradkin, V. J. Emery, Electronic liquid-crystal phases of a doped Mott insulator. *Nature* **393**, 550-553 (1998).
4. V. Oganesyan, S. A. Kivelson, E. Fradkin, Quantum theory of a nematic Fermi fluid. *Phys. Rev. B* **64**, 195109 (2001).
5. E. Fradkin, S. A. Kivelson, M. J. Lawler, J. P. Eisenstein, A. P. Mackenzie, Nematic Fermi fluids in condensed matter physics. *Ann. Rev. Cond. Mat. Phys.* **1**, 153-178 (2010).
6. E. W. Carlson, K. A. Dahmen, Using disorder to detect locally ordered electron nematics via hysteresis. *Nature Commun.* **2,** 379 (2011).
7. B. V. Phillabaum, E. W. Carlson, K. A. Dahmen, Spatial complexity due to bulk electronic nematicity in a superconducting underdoped cuprate. *Nature Commun.* **3,** 915 (2011).
8. Y. Ando, K. Segawa, S. Komiya, A. N. Lavrov, Electrical resistivity anisotropy from self-organized one dimensionality in high-temperature superconductors. *Phys. Rev. Lett.* **88**, 137005 (2002).
9. V. Hinkov *et al.*, Electronic liquid crystal state in the high-temperature superconductor $YBa_2Cu_3O_{6.45}$. *Science* **319**, 597-601 (2008).
10. M. J. Lawler *et al.*, Intra-unit-cell electronic nematicity of the high-T_c copper-oxide pseudogap states. *Nature* **466**, 347-351 (2010).

11. R. Daou *et al.*, Broken rotational symmetry in the pseudogap phase of a high-T_c superconductor. *Nature* **463**, 519-522 (2010).

12. K. Fujita *et al.*, Simultaneous transitions in cuprate momentum-space topology and electronic symmetry breaking. *Science* **344**, 612-616 (2014).

13. Y. Lubashevsky, L. D. Pan, T. Kirzhner, G. Koren, N. P. Armitage, Optical birefringence and dichroism of cuprate superconductors in the THz regime. *Phys. Rev. Lett.* **112**, 147001 (2014).

14. O. Cyr-Choinière *et al*., Two types of nematicity in the phase diagram of the cuprate superconductor $YBa_2Cu_3O_y$. *Phys. Rev. B* **92**, 224502 (2015).

15. J.-C. Zhang *et al.*, Anomalous thermal diffusivity in underdoped $YBa_2Cu_3O_{6+x}$. *Proc. Natl. Acad. Sci. USA* **114,** 5378-5383 (2017).

16. Y. Sato *et al.*, Thermodynamic evidence for a nematic phase transition at the onset of the pseudogap in YBa_2Cu_3Oy. *Nature Physics* **13**, 1074-1078 (2017).

17. J. Wu, A.T. Bollinger, X. He, I. Božović, Spontaneous breaking of rotational symmetry in copper oxide superconductors. *Nature* **547**, 432-435 (2017).

18. J.-H. Chu *et al.*, In-plane resistivity anisotropy in an underdoped iron arsenide superconductor. *Science* **329**, 824–826 (2010).

19. T.-M. Chuang *et al.*, Nematic electronic structure in the "parent" state of the iron-based superconductor $Ca(Fe_{1-x}Co_x)_2As_2$. *Science* **327**, 181-184 (2010).

20. R. M. Fernandes, A. V. Chubukov, J. Schmalian, What drives nematic order in iron-based superconductors? *Nat. Phys.* **10**, 97-104 (2014).

21. S. Kasahara *et al.*, Electronic nematicity above the structural and superconducting transition in $BaFe_2(As_{1-x}P_x)_2$. *Nature* **486**, 382-385 (2012).

22. F. Ronning *et al.*, Electronic in-plane symmetry breaking at field-tuned quantum criticality in $CeRhIn_5$. *Nature* **548**, 313-317 (2017).

23. C. M. Varma, L. Zhu, Helicity order: hidden order parameter in URu_2Si_2. *Phys. Rev. Lett.* **96**, 036405 (2006).

24. A. P. Mackenzie *et al.*, Extremely strong dependence of superconductivity on disorder in Sr_2RuO_4. *Phys. Rev. Lett.* **80**, 161-164 (1998).

25. A. Steppke *et al.*, Strong peak in T_c of Sr_2RuO_4 under uniaxial pressure. *Science* **355**, 148 (2017).

26. The indices used (also by the substrate vendor) for the $NdGaO_3$ substrate refer to orthorhombic indices (*Pbnm* setting), where the long axis of $NdGaO_3$ is the [001] direction. Similarly, LSAT is referred to with pseudo-cubic indices even though it is in fact tetragonal but the distortion is so small that it is difficult to discern and is generally ignored.

27. M. Steins, J. Doerschel, P. Reiche, Crystal structure of aluminium lanthanum strontium tantalum oxide, $(La_{0.272}Sr_{0.728})(Al_{0.648}Ta_{0.352})O_3$. *Z. Kristallogr. - New Cryst. Struct.* **212**, 77 (1997).

28. H. P. Nair *et al.*, Demystifying the growth of superconducting Sr_2RuO_4 thin films. *APL Materials* **6**, 101108 (2018).

29. T. M. Rice, M. Sigrist, Sr_2RuO_4: an electronic analogue of ^{3}He? *J. Phys. Condens. Matter* **7**, L643 (1995).

30. Y. Maeno *et al.*, Superconductivity in a layered perovskite without copper. *Nature* **372**, 532-524 (1994).

31. A. P. Mackenzie, Y. Maeno, The superconductivity of Sr_2RuO_4 and the physics of spin-triplet pairing. *Rev. of Mod. Phys.* **75**, 657-712 (2003).

32. Y. Maeno, S. Kittaka, T. Nomura, S. Yonezawa, K. Ishida, Evaluation of spin-triplet superconductivity in Sr_2RuO_4. *J. Phys. Soc. Jpn* **81**, 1-29 (2012).

33. A. P. Mackenzie, T. Scaffidi, C.W. Hicks, Y. Maeno, Even odder after twenty-three years: the superconducting order parameter puzzle of Sr_2RuO_4. *Npj Quantum Materials* **2**, 40 (2017).

34. A. Pustogow *et al.*, Pronounced drop of ^{17}O NMR Knight shift in superconducting state of Sr_2RuO_4. http://arXiv:1904.00047 [cond-mat.supr-con] (2019).

35. W.R. Busing, H. A. Levy, Angle calculations for 3- and 4- circle X-ray and neutron diffractometers. *Acta Cryst.* **22**, 457 (1967).

36. Chinkyo Kim, "Strain Relaxation Mechanism of Semiconductor Thin Films." PhD Thesis, University of Illinois, Urbana (1998).

37. L. J. van der Pauw, A method of measuring specific resistivity and Hall effect of discs of arbitrary shape. *Philips Res. Rep.* **20**, 220–224 (1958).

38. J. F. Nye, *Physical Properties of Crystals: Their Representation by Tensors and Matrices.* Oxford University Press (1957, 1985).

39. L. J. van der Pauw, Determination of resistivity tensor and Hall tensor of anisotropic conductors. *Philips Res. Rep.* **16**, 187–195 (1961).

40. H. C. Montgomery, Method for measuring electrical resistivity of anisotropic materials. *J. Appl. Phys.* **42,** 2971–2975 (1971).

41. M. A. Zurbuchen *et al*., Morphology, structure, and nucleation of out-of-phase boundaries (OPBs) in epitaxial films of layered oxides. *J. Mater. Res.* **22** 1439–1471 (2007).

42. M. A. G. Halliwell, S. J. Chua, Determining substrate orientation using a high-resolution diffractometer. *Journal of Crystal Growth* **192**, 456-461 (1998).

Acknowledgments: We thank A. Mackenzie and A. Gozar for valuable discussions. **Funding:** The research at Brookhaven National Laboratory was supported by the US Department of Energy, Basic Energy Sciences, Materials Sciences and Engineering Division. X.H. is supported by the Gordon and Betty Moore Foundation's EPiQS Initiative through grant GBMF4410. H.P.N., N.J.S., K.M.S., and D.G.S. acknowledge support from the National Science Foundation (Platform for

Accelerated Realization, Analysis and Discovery of Interface Materials (PARADIM)) under Cooperative Agreement No. DMR-1539918 and from the W.M. Keck Foundation. N.J.S. acknowledges support from the National Science Foundation Graduate Research Fellowship Program under Grant No. DGE-1650441. This research is funded in part by the Gordon and Betty Moore Foundation's EPiQS Initiative through Grant No. GBMF3850 to Cornell University. Substrate preparation was performed in part at the Cornell NanoScale Facility, a member of the National Nanotechnology Coordinated Infrastructure (NNCI), which is supported by the NSF (Grant No. ECCS-1542081). **Author contributions:** MBE synthesis was performed by H.P.N. and N.J.S. with advice from D.G.S. and K.M.S., lithography by A.T.B., transport measurements by J.W., and X-ray diffraction by I.R. The project was conceived and led by I.B. and D.S. All authors contributed to the manuscript. **Competing interests:** Authors declare no competing interests. **Data and materials availability:** Data needed to evaluate the conclusions of this manuscript are presented in the main text and supplementary materials.

Supplementary Materials:

Materials and Methods

Figures SF1-SF5

Tables ST1-ST3

References (*35-42*)

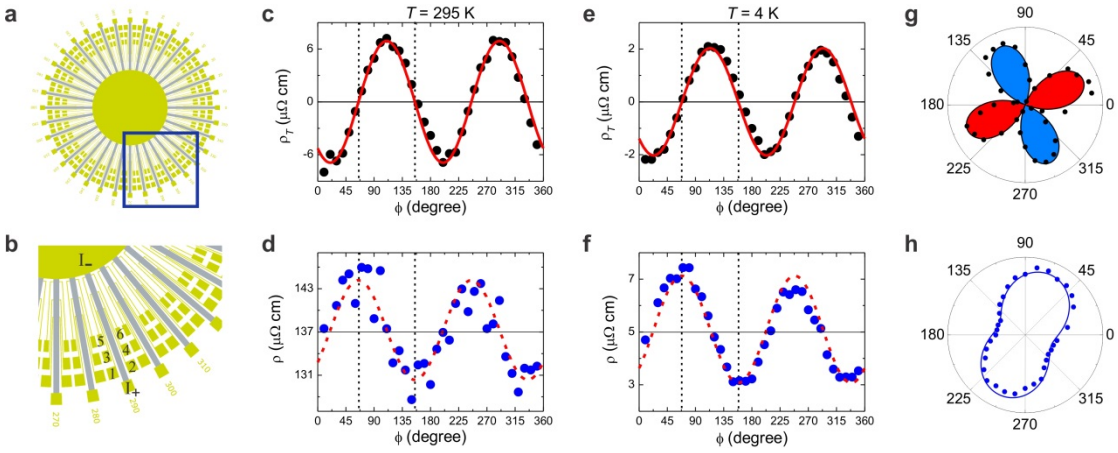

Figure 1. Angular dependence of the transverse (ρ_T) and longitudinal (ρ) resistivity of the tetragonal SRO film on the LSAT substrate.

In ultrathin SRO films, as determined by the high-resolution X-ray diffraction experiments, the in-plane lattice constants *a* and *b* are epitaxially anchored to those of the substrate. Their difference is tiny (less than 0.03%) in SRO grown on tetragonal LSAT substrates.

a, A schematic drawing of the lithography pattern used in this study. 36 identical Hall bars are drawn in steps of $\Delta\phi = 10^0$ to cover the whole range from 0^0 to 360^0.
b, On each Hall bar, the current runs from the contact I+ to the contact I-. The longitudinal voltages are recorded using pairs like {1,3} and {3,5}, and the transverse voltages using the pairs {1,2}, {3,4} and {5,6}.
c, The measured transverse resistivity ρ_T (black dots) at T = 295 K fits well (the solid red curve) to $\rho_T(\phi) = \rho_T^0 \sin[2(\phi-\alpha)]$, with $\alpha = 65°$. The black dashed lines mark the angles at which $\rho_T(\phi)$ cross zero.
d, The measured longitudinal resistivity $\rho(\phi)$ (blue diamonds) at T = 295 K is well reproduced (the dashed red line) by shifting the fitted $\rho_T(\phi)$ curve upwards by a constant, $\bar{\rho}$, and left by 45^0. The black dashed lines are aligned with those in **c** and correspond to the angles $\rho(\phi)$ manifest maximum or minimum values, evidencing the correlation between $\rho_T(\phi)$ and $\rho(\phi)$.
e, The same as in **c** but for T = 4 K.
f, The same as in **d** but for T = 4 K.
g, The same as in **e**, but plotted in polar coordinates; the experimental data (black dots) and the fitted curve (the solid line). Blue filling indicates positive and red negative values.
h, The same as in **f**, in polar coordinates.

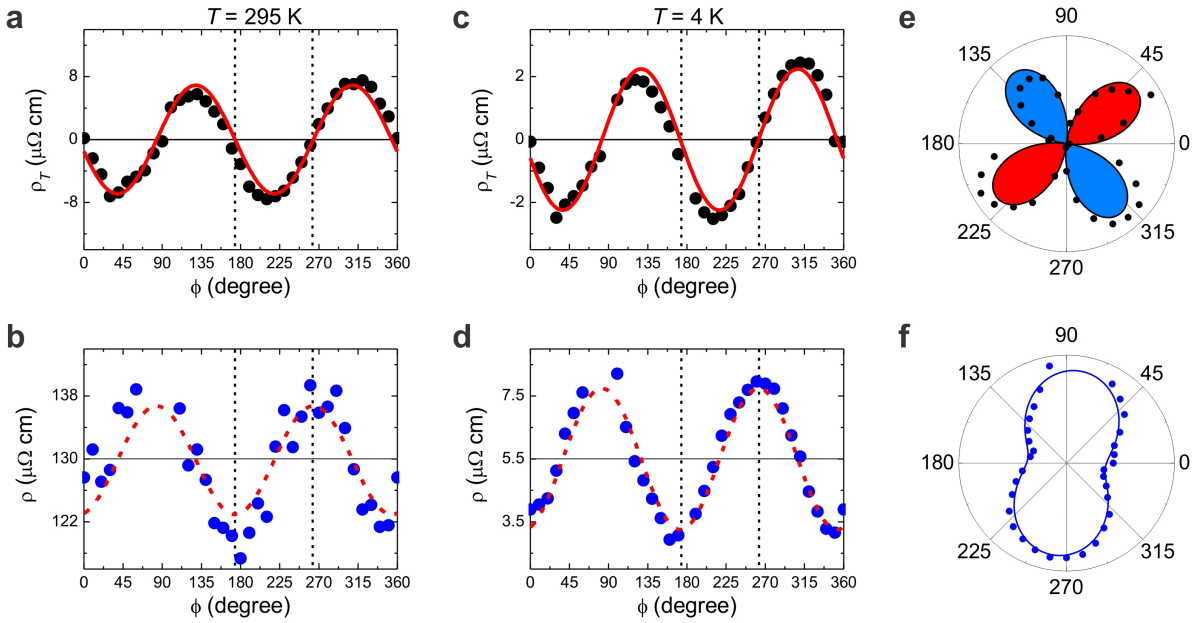

Figure 2. $\rho_T(\phi)$ and $\rho(\phi)$ of orthorhombic SRO film on (110) NGO substrate.

In ultrathin SRO films grown on orthorhombic (110) NGO substrates, the difference between *a* and *b* lattice constants is 0.5%, an order of magnitude larger than in SRO films on LSAT.

a, The $\rho_T(\phi)$ data (black dots) measured at T = 295 K and the fit (solid red curve) to $\rho_T(\phi) = \rho_T^0 \sin[2(\phi-\alpha)]$, with α = -6°. The black dashed lines are defined the same way as in Fig. 1.
b, The $\rho(\phi)$ data (blue diamonds) measured at T = 295 K are well reproduced (the dashed red line) by the curve obtained by fitting $\rho_T(\phi)$, and shifted upwards by a constant, $\bar{\rho}$, and left by 45^0.
c, The same as in **a** but for T = 4 K.
d, The same as in **b** but for T = 4 K.
e, The same as in **c** but plotted in polar coordinates; the experimental data (black dots) and the fitted curve (the red solid line). Blue filling indicates positive and red negative values.
f, The same as in **d,** in polar coordinates.

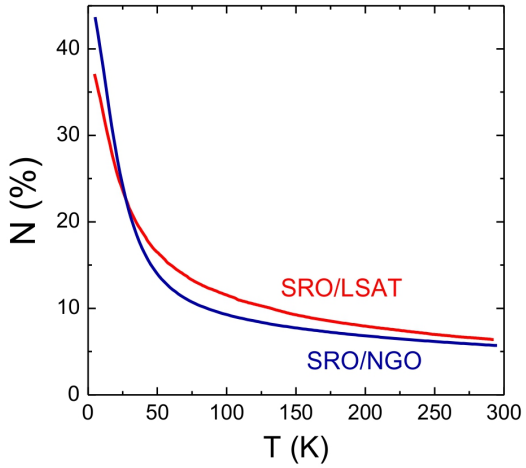

Figure 3. Temperature dependence of the nematicity magnitude *N* in the SRO/LSAT and SRO/NGO samples. In analogy to the Hall angle, the magnitude of nematicity is defined as $N = \rho_T^0/\bar{\rho}$. It increases as *T* decreases in both samples, indicating that the ground state of SRO is electronic nematic. At any temperature below 300 K, the values of *N* in SRO/LSAT and SRO/NGO are close to one another, despite the fact that the orthorhombic distortion is more than an order-of-magnitude larger (0.5%) in SRO/NGO than in SRO/LSAT (0.03%). Apparently, the lattice distortion only affects the director (i.e., the orientation of nematicity) but has almost no effect on nematicity magnitude.

Supplementary Materials for

Title: Electronic nematicity in Sr_2RuO_4

J. Wu[1,*], H. P. Nair[2,*], A. T. Bollinger[1], X. He[1,3], I. Robinson[1], N. J. Schreiber[2], K. M. Shen[4,5], D. G. Schlom[2,5], and I. Božović[1,3]

Correspondence to: bozovic@bnl.gov

This PDF file includes:

Materials and Methods
Supplementary Text
Figs. SF1 to SF5
Tables ST1 to ST3

Materials and Methods

Materials

High-quality single crystal films of (001)-oriented SRO were synthesized in a Veeco GEN10 molecular-beam epitaxy system. Well-oriented 10 mm × 10 mm × 1 mm single-crystal substrates of (110) $NdGaO_3$ and (001) $(LaAlO_3)_{0.29}$–$(Sr_{1/2}Al_{1/2}TaO_3)_{0.71}$ (LSAT) from CrysTec GmbH (*32*,*33*) were heated to growth temperatures in the range 870 °C to 910 °C, as measured by an optical pyrometer operating at 1550 nm. There they were exposed to molecular beams of strontium (99.99% purity), ruthenium (99.99% purity), and distilled ozone (~80% O_3 + 20% O_2 made from oxygen gas with 99.994% purity), all supplied at the same time (co-deposition). The strontium and ruthenium fluxes ranged from about 1.9×10^{13} to 3.3×10^{13} atoms·cm^{-2}s^{-1} and 1.4×10^{13} to 2.5×10^{13} atoms·cm^{-2}s^{-1}, respectively, corresponding to an excess ruthenium flux of about 2×10^{12} to 9×10^{12} atoms·cm^{-2}s^{-1} for the growth of Sr_2RuO_4. The growth rate of the Sr_2RuO_4 films ranged from 0.09 Å/s to 0.16 Å/s. To facilitate radiative coupling between the SiC substrate heater filament and the substrates, the back sides of the substrates were coated with a 10 nm thick titanium adhesion layer followed by 400 nm of platinum followed by 200 nm of polycrystalline $SrRuO_3$. The background oxidant pressure during growth ranged from of 8×10^{-7} Torr to 1×10^{-6} Torr. At the completion of growth, the strontium and ruthenium shutters were simultaneously closed, and the film was rapidly cooled to below 250 °C in the same pressure of distilled ozone in which it was grown. Strontium was evaporated from a low-temperature cell while an electron-beam evaporator was used for ruthenium. Additional details, including the growth window for the adsorption-controlled conditions used, may be found elsewhere *(34)*.

The best of our SRO films are superconducting with the critical temperature $T_c \approx 1.5$ K, as high as in the best bulk SRO crystals *(34)*.

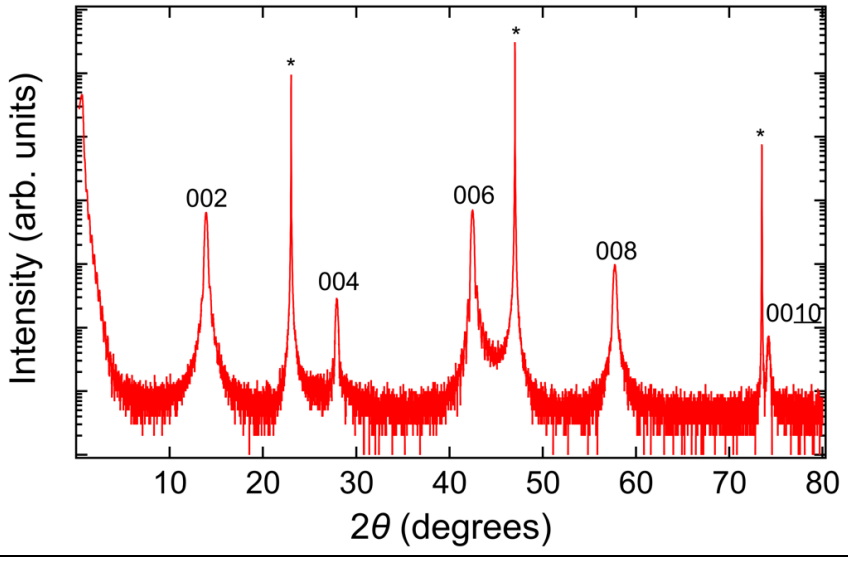

Fig. SF1. **X-ray diffraction θ-2θ scan of a ~30 nm thick (001)-oriented Sr_2RuO_4 film grown on a $NdGaO_3$(110) substrate.** All of the peaks in the scan can be indexed to either the film or the substrate (asterisks).

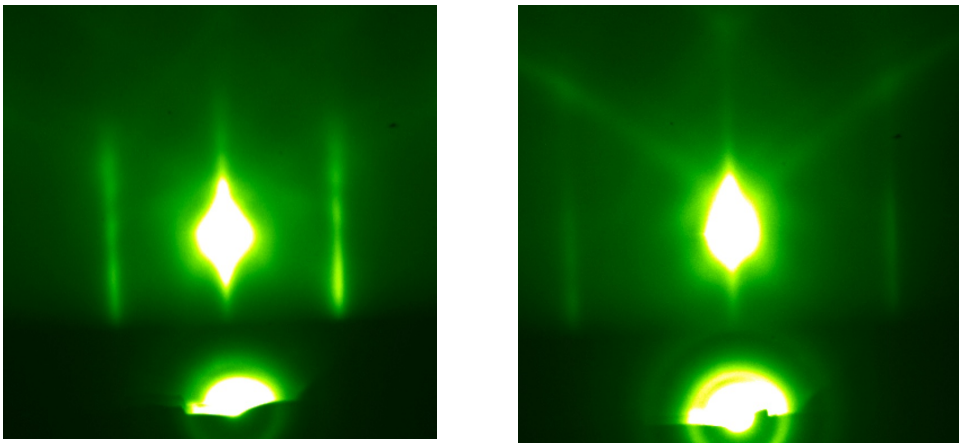

Fig. SF2. Reflection high-energy electron diffraction (RHEED) from the same film. **a,** The RHEED pattern recorded with the electron beam incident along the <100> azimuth of the Sr_2RuO_4 thin film. **b,** the same, but with the beam incident along the <110> azimuth. The RHEED patterns were recorded at a substrate temperature of 300 ˚C at the end of the growth.

Methods

The SRO films were patterned by standard photo-lithography procedures to form the "sun-beam" pattern shown in Fig.1a. The precision in the alignment of lithography is ±1 μm. The electric current runs along a chosen Hall bar at a time with the corresponding longitudinal or transverse voltages being recorded using three pairs of evenly-spaced gold contacts (Fig. 1b) on the Hall bar. The angle $\Delta\phi$ between two successive Hall bars is 10^0 and the total of 36 Hall bars systematically map out the in-plane angle ϕ from 0^0 to 350^0. The orientation of the Hall bar with the initial angle $\phi = 0^0$ is aligned with the [0 0 1] crystal axis of SRO lattice with a precision of 0.1^0.

The transport measurements were carried out in both Helium-4 and Helium-3 cryogenics to study the temperature dependence of longitudinal and transverse resistivity. The thermal stability of both systems is better than ±1 mK.

Supplementary Text

1. Lattice orthorhombicity determined by XRD

Single crystal X-ray diffraction was used to determine the lattice constants of the SRO films on the two substrates, NGO and LSAT. An in-house Bruker D8 4-circle diffractometer was used to locate the angular positions of a number of peaks from the films using λ = 1.540 Å, 0.5 mm resolution-defining slits and a 1 mm out-of-plane detector slit to provide 3D resolution. Following the standard angle convention of Busing and Levy (*35*), for each reflection the detector angle (2θ), the sample angle (θ) and the tilt Euler angle (χ) were scanned in sequence until consistent, while the azimuthal Euler angle (ϕ) was kept fixed. The peak center positions of seven accessible reflections were least-squares-fit to a general lattice without constraints to determine the lattice constants (*37*). The self-consistency of the fit was used to generate an absolute error, the distance

in reciprocal space between the reciprocal lattice point and its measured position. These errors were then used as a conservative estimate of the accuracy of the measured lattice constants.

Tables ST1 and ST2 show the measured angles and the resulting errors for the least-squares fit. It is clear that the errors are well distributed and at the level expected for a slit-defined instrument. Table ST1 shows the measured lattice parameters of SRO films grown on LSAT substrate. The LSAT is less precisely measured, but consistent with $a = b$, or a tetragonal structure of the film. Table ST2 shows the measured lattice parameters of SRO films grown on NGO substrate. The measured values of a and b for SRO on NGO are no longer consistent with $a = b$, so we conclude this film to be orthorhombic.

H	K	L	2 θ	θ	φ	χ	Error (Å^{-1})
1	-1	4	43.50	21.760	-46.26	40.61	0.0039
-1	1	4	43.50	21.761	133.51	40.64	0.0039
-1	-1	4	43.51	21.770	223.52	40.76	0.0025
1	1	4	43.53	21.766	43.71	40.50	0.0047
0	1	3	31.23	15.619	88.60	42.46	0.0067
-1	0	3	31.23	15.622	178.45	42.53	0.0045
1	0	3	31.23	15.619	-1.21	42.41	0.0055

Table ST1. The measured diffractometer angles (*SR1*) and the resulting errors to the least-squares fit for SRO films on LSAT.

H	K	L	2 θ	θ	φ	χ	Error (Å^{-1})
-1	0	3	31.31	15.566	225.50	42.11	0.0020
0	1	3	31.22	15.607	135.51	42.12	0.0030
1	0	3	31.31	15.649	45.65	42.05	0.0025
0	-1	3	31.26	15.614	-44.44	42.36	0.0036
1	1	4	43.55	21.787	90.50	40.37	0.0021
-1	1	4	43.58	21.771	180.46	40.34	0.0037
1	-1	4	43.56	21.787	0.73	40.45	0.0038

Table ST2. The measured diffractometer angles (*SR1*) and the resulting errors to the least-squares fit for SRO films on NGO.

Substrate	a	b	c	α	β	γ	Volume (Å^3)
LSAT	3.873(11)	3.874(11)	12.75(4)	90.09	89.98	90.01	190

NGO	3.848(7)	3.861(7)	12.79(2)	90.00	89.99	89.95	191

Table ST3. Measured lattice parameters of SRO films on the two different substrates. Errors estimated from the misfit of the lattice are shown in parentheses.

2. Pitfalls of using the van der Pauw method to probe nematicity

The van der Pauw method is commonly used to measure the resistivity of single crystals. This method, as it was originally conceived and most widely utilized (*36*) is appropriate for measuring the resistivity of materials with isotropic in-plane conductivity. For materials with anisotropic resistivity, e.g., when it is desired to probe for electronic nematicity, this approach has pitfalls of which one should be aware (*38*). Below is an example that illustrates the subtlety.

On a uniform as-grown SRO film on an (110) NGO substrate, four point contacts were wire-bonded onto the four corners to carry out the van der Pauw measurements. The recorded $R(T)$ along two orthogonal directions [001] and [010] manifest significant difference (Fig. SF3a), confirming $R_a \neq R_b$ and consequently the nematicity. Intuitively, one would expect that the magnitude of the nematicity N should be proportional to ΔR ($= R_a - R_b$). If that were true, N should first decrease with sample cooling until it vanishes at $T \sim 40$ K, and on further cooling N should increase, but with the opposite sign. This inferred peculiar $N(T)$ behavior is, however, merely an artifact due to misinterpretation of the van der Pauw method. To illustrate this, we patterned the same SRO film with the sun-beam lithography pattern (Fig. 1a) and measured the longitudinal resistivity ρ along the same [001] and [010] directions. One can see that $\rho_a \neq \rho_b$, i.e., the electronic state is nematic, consistent with Fig. SF3a. Remarkably, the $\rho_a(T)$ and ρ_b T) do not cross at any T from 295 K down to 4 K (Fig. SF3b). The calculated $N(T)$ does not change sign at any temperature; it monotonically increases as T decreases, similar to $N(T)$ shown in Fig. 3.

The merit of the sun-beam method is that the excitation current is guided by the Hall bar geometry to run uniformly along a given direction (*17*). Conversely, in the van der Pauw method, the current density $\boldsymbol{j}$ between two current contacts varies locally in both direction and amplitude. More importantly, the spatial distribution of $\boldsymbol{j}$ is susceptible to the magnitude of the nematicity. Thus, the correct interpretation of the measured R_a and R_b demands a delicate self-consistent modeling of $\boldsymbol{j}$ under the influence of the unknown N. It is clear that the dependence of R on N can be approximated as a collinear function only under the extreme condition if N is so tiny that the influence of the nematicity is negligible to $\boldsymbol{j}$ and the usual van der Pauw analysis applies. Generally, R does not bear a simple relation to N.

We note that van der Pauw (*39*), Montgomery (*40*) and others recognized this limitation and developed variants of the original van der Pauw method that are appropriate for measuring electronic nematicity. Unfortunately, these latter methods require either six planar samples of known and distinct orientation (*39*) or *a priori* knowledge of the principal axes (*40*), making them inappropriate for a study of a single thin film.

Nevertheless, we applied this method to analyze the resistance data shown in Fig. SF3a and calculated the longitudinal resistivity along the same [001] and $[1\ \bar{1}\ 0]$ directions respectively (Fig. SF3c). The two $\rho(T)$ curves plotted in Fig. SF3c show no crossings, in stark contrast to the two R(T) curves in Fig. SF3a, but in qualitative agreement with the $\rho(T)$ curves in Fig. SF3b. This confirms that the crossing in Fig. SF3a is merely an artifact, due to the fact that the nematic director

is not aligned with either the *a* or *b* axes. The quantitative values of $\rho(T)$ in Fig. SF3c at a fixed temperature, e.g. T = 295 K, are fairly close to those of $\rho(T)$ in Fig. SF3b. The magnitude of the nematicity, determined by the difference between the two $\rho(T)$ curves, are nearly the same in Fig. SF3b and Fig. SF3c at 4.2 K, but gets underestimated in Fig. SF3c at elevated temperatures.

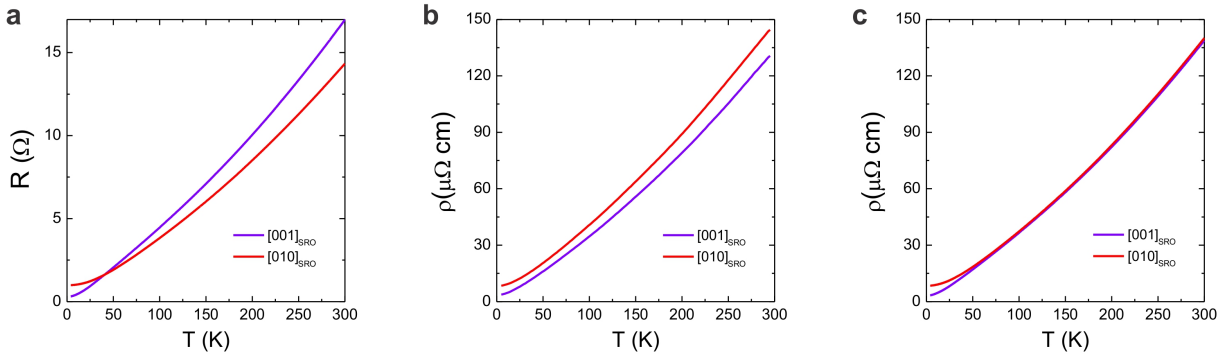

Fig. SF3. A comparison of the van der Pauw and the sunbeam-pattern methods. **a,** The longitudinal resistances of SRO grown on (110) NGO were measured along [001] and [1 $\overline{1}$ 0] directions of NGO respectively, by the van der Pauw method. **b,** On the same sample after being patterned by the sun-beam lithography pattern, the longitudinal resistivities were again measured. **c**, The longitudinal resistivity along [001] and [1 $\overline{1}$ 0] were calculated from the resistance data in **a**, based on the van der Pauw method generalized to anisotropic materials (*36*).

To avoid the complexity in analysis and modeling, the sun-beam method is clearly preferable. Moreover, for the more general case in which the director of the nematicity does not align with the crystal *a* or *b* axis, e.g., in SRO films grown on LSAT (Fig. 1), the interpretation of the van der Pauw method gets less straightforward. For instance, if the director of the nematicity is along [110] direction of SRO, then the measured $R_a = R_b$, misleading one to infer that the nematicity is zero. Therefore, the angular resolution of the sun-beam method is pivotal to ensure the accurate characterization of nematicity.

3. Robustness of superconductivity and electronic nematicity

The electronic nematicity is present in SRO films on both LSAT and NGO substrates at room temperature and its magnitude increases with decreasing temperature. For the SRO film grown on a (110) NGO substrate, superconductivity was observed at low temperatures with the onset T_c = 0.9 K (Fig. SF4a). By adjusting the growth condition slightly off the optimal, we introduced more defects into the film and suppressed superconductivity so that no transition is observed (Fig. SF4c) down to 0.3 K. On the other hand, the angular dependence of $\rho_T(\phi)$ of both films manifest 180^0 oscillations and possess a very similar "clover-leaf" shape when plotted in polar coordinates (Figs. SF4b and SF4d). This comparison clearly shows that the electronic nematicity in the normal state of SRO is robust against the disturbance caused by structural defects and the demise of the superconductivity. Nematicity is intrinsic to SRO films.

4. The substrate miscut is not the root cause of the observed nematicity

Restricted by the precision in the alignment during polishing, the surface of a substrate, e.g. LSAT, inevitably deviates from the ideal crystallographic {001} plane by a tiny miscut angle. The upper limit of the miscut for the substrates used is 0.2 degree. The atomic steps at the SRO/LSAT and SRO/NGO interfaces, and the concomitant out-of-phase boundaries in the SRO film (*41*), in principle violate the $\mathbf{C}_4$ rotational symmetry. Traversing the steps and out-of-phase boundaries can increase the electronic scattering rate, so the in-plane resistivity could be larger in that direction. In addition, note that SRO is a layered material and has a considerable in-plane vs. out-of-plane anisotropy so one could also increase the measured resistivity in the direction perpendicular to the substrate steps by picking up some *c*-axis component. If this were indeed the case, there should be a one-to-one correspondence between the step orientation and the nematic director; resistivity should always be the lowest in the direction parallel to the steps.

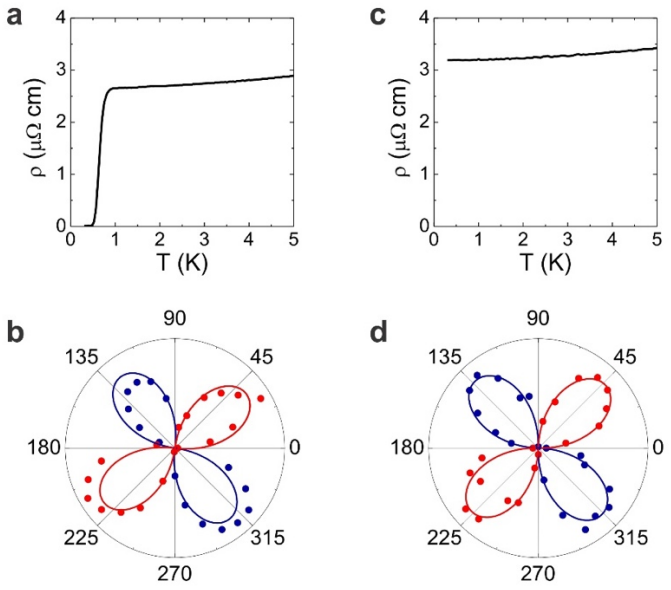

Fig. SF4. **The magnitude of nematicity is nearly the same in superconducting and non-superconducting SRO films. a,** the longitudinal resistivity $\rho(T)$ shows superconductivity with $T_c \approx 0.9$ K. **b,** $\rho_T(\phi)$ at $T = 295$ K in the same sample, plotted in polar coordinates. **c,** $\rho(T)$ of a non-superconducting film with a higher residual resistivity. **d,** $\rho_T(\phi)$ of the non-superconducting film.

This motivated us to explore whether the orientation and density of the atomic steps are related to the measured anisotropy in the SRO films. Since the miscut varies randomly from one substrate to another, the resulting atomic steps vary in density and orientation. By choosing substrates with different miscut and synthesizing SRO films under identical conditions, we can make a one-on-one comparison between the orientation of the anisotropy and the miscut. Since traversing the steps and out-of-phase boundaries can only increase the electronic scattering rate, and

consequently the longitudinal resistivity, the in-plane direction parallel to the atomic steps should correspond to the direction in which the resistivity $\rho(\phi)$ reaches its minimum ρ^{min}.

The direction and magnitude of the substrate miscut was measured by XRD using the technique outlined in (*42*). In Fig. SF5, we show the measured orientation of the atomic steps, denoted by the green arrows, for five SRO films grown on (110) NGO substrates. (The horizontal axis in all plots is aligned with the [001] axis of NGO, i.e., it is in the direction with the shorter lattice constant in the NGO substrate and the SRO film.) For comparison, the orientation of the nematic director, i.e., the angle corresponding to $\rho^{min}(\phi)$, is indicated by the black arrows. It is clear there is no one-to-one correspondence between the orientations of substrate steps and of the nematic director.

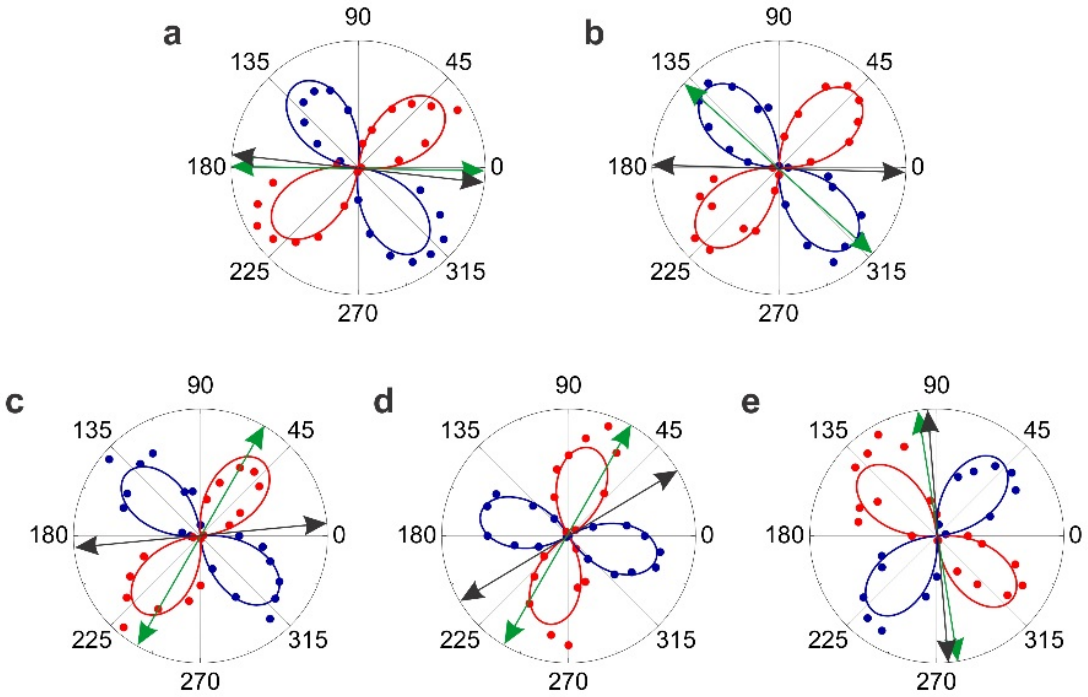

Fig. SF5. **In SRO films grown on NGO(110) under identical growth conditions, the orientation of substrate steps (green arrows) does not coincide with that of the nematic director (black arrows). a,** The miscut angle of the substrate is $\theta = 0.05^0$. **b,** $\theta = 0.06^0$. **c,** $\theta = 0.038 \pm 0.001^0$. **d,** $\theta = 0.140 \pm 0.002^0$. **e,** $\theta = 0.16 \pm 0.01^0$. The horizontal axis in all plots is along the direction with [001] the shorter lattice constant in the NGO substrate and the SRO film.

Moreover, an even stronger argument against this model is its dramatic failure to account quantitatively for the magnitude of the observed effect. In principle, given the large out-of-plane vs. in-plane resistivity anisotropy in SRO (of the order of 1,000:1), the substrate miscut could cause some admixture of the c-axis resistivity if the current is running along the miscut direction. To estimate the magnitude of this effect, one needs to know the miscut angles, so these were measured and are indicated in the caption to Fig. SF5 for each of the five films. The smallest of

these is $\theta = 0.038 \pm 0.001^0$ (Fig. SF5c) and in this case, the 'step model' would predict $N = 0.03\%$, three orders of magnitude less than what we see. And even for the largest miscut value, $\theta = 0.16 \pm 0.01^0$ (Fig. SF5e), the predicted N would be less than 1%, still too low by a factor of 40.

5. Temperature dependence of ρ and ρ_T

Representative plots of the temperature dependence of ρ and ρ_T for the SRO film grown on LSAT substrate are shown in Fig. SF6. The three angles ϕ are chosen so that $\rho(\phi)$ is at the maximum (70^0), middle (110^0), and minimum (160^0), see Fig. 1d and 1f for the $\rho(\phi)$ plot. It is clear from Fig. SF6 that $\rho(T)$ is parabolic, in contrast to the nearly-linear $\rho_T(T)$ behavior. This difference is also illustrated in Fig. SF6c. Apparently, the ratio ρ/ρ_T is not constant, unambiguously showing that ρ and ρ_T are two independent physical quantities.

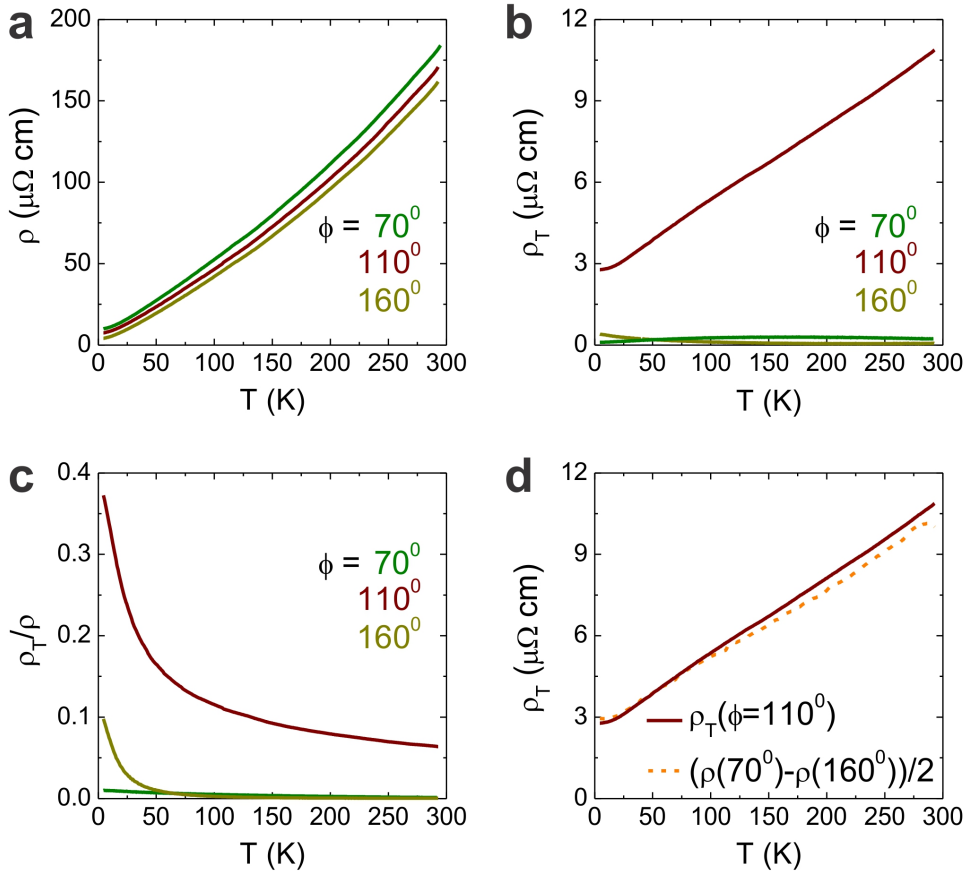

Fig. SF6. Temperature dependence of ρ and ρ_T of the SRO film on LSAT substrate. a, the longitudinal resistivity $\rho(T)$ at three angles corresponding to the maximum (70^0), middle (110^0), and minimum (160^0) of $\rho(\phi)$. **b,** $\rho_T(T)$ at these three angles. **c,** the ratio ρ/ρ_T is not a constant, showing that ρ_T is indeed not proportional to ρ, thus ruling out the possibility that the observed transverse voltage is due to misalignment of the voltage contacts. **d,** $\rho_T(\phi=110^0)$ is essentially equal to $(\rho_T(\phi=70^0) - \rho_T(\phi=160^0))/2$, as expected from equations (1) and (2). This shows that the origin of the transverse voltage is the anisotropy of ρ(T), i.e., the electronic nematicity.

The correlation between ρ and ρ_T is given by the equations (1) and (2) in the main text. One consequence following these equations is the prediction that $\rho_T^0 = \Delta\rho = (\rho_{max} - \rho_{min})/2$. Here, at every temperature, $\rho_{max} = \rho(\phi = 70^0)$ and $\rho_{min} = \rho(\phi = 160^0)$, respectively. Meanwhile, ρ_T^0 corresponds to $\phi = 110^0$, the angle at which $\rho(\phi)$ reaches the average $\bar{\rho}$ while $\rho_T(\phi)$ reaches the maximum (see Fig. 1). Therefore, it can be inferred that $\rho_T(\phi = 110^0) = (\rho(\phi = 70^0) - \rho(\phi = 160^0))/2$. Indeed, this non-trivial relation is clearly confirmed in Fig. SF6d. This is another strong evidence that the unusual transverse resistivity ρ_T originates from the electronic nematicity.

6. Ruling out the artifacts of lithography: $\rho_T(\phi)$ in the control-sample Ti film

In order to test the (unlikely) possibility that our lithography and measurements may be the cause of the observed angular oscillations in $\rho_T(\phi)$, we performed a full ARTR study of a thin Ti film, chosen as a control sample. Ti is a well-known conventional metal and should not be an electronic nematic. Thus, for the Ti film, $\rho_T(\phi)$ should not oscillate with ϕ; rather, it should be zero at every angle, by symmetry. Whether or not this is observed in our experiments is a decisive test of our ARTR methodology and of any artifacts due to lithography and measurement technique.

A 16 nm thick Ti film was deposited on (001) Si substrate by e-beam evaporation and patterned by the standard photolithography to form the sun-beam pattern as shown in Figs. 1a and 1b. ARTR measurements were carried out on the patterned Ti film, following exactly the same procedure as for the SRO films, in particular using the same lithography mask and the same measurement setup. To compare Ti and SRO films on the same footing, we normalized the measured $\rho_T(\phi)$ by the corresponding average longitudinal resistivity $\bar{\rho}$ for Ti and SRO films, respectively. The results are shown in Fig. SF7. Apparently, $\rho_T(\phi)$ in the Ti film shows no oscillations and is equal to zero within the experimental uncertainty. This is in stark contrast to $\rho_T(\phi)$ in the SRO film. Therefore, it seems quite definite that our lithography and measurement methodology are not the cause of the observed breaking of the rotational symmetry in SRO films.

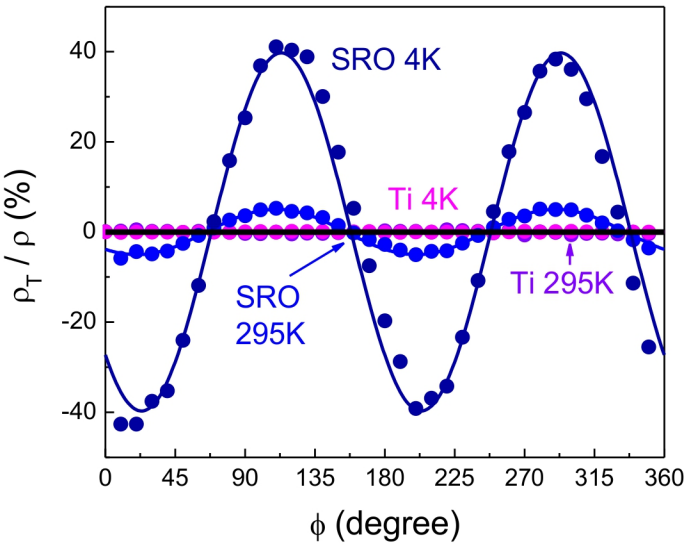

Fig. SF7. **Comparison of SRO with the Ti control sample.** In Ti film, $\rho_T(\phi)$ shows no angular oscillations at $T = 295$ K (purple dots) nor at $T = 4$ K (magenta dots). This is in stark contrast to $\rho_T(\phi)$ of the SRO film

grown on the LSAT substrate (T = 295 K, lighter blue dots; T = 4 K, darker blue dots). The measured $\rho_T(\phi)$ is normalized by the average longitudinal resistivity $\bar{\rho}$ for the respective films, in order to facilitate the comparison. The solid lines are the best fits to $\rho_T(\phi) = \rho_T^0 \sin[2(\phi-\alpha)]$ for experimental data in the corresponding color. The solid black line stands for $\rho_T(\phi)/\bar{\rho} = 0$